The Pennsylvania State University

The Graduate School

LINEAR DYNAMIC PRESSURE EXPLAINS THE PERSISTENCE OF SUPERCELL REAR FLANK DOWNDRAFTS

A Thesis in

Meteorology and Atmospheric Science

by

Samuel Brandt

Submitted in Partial Fulfillment
of the Requirements
for the Degree of

Master of Science

August 2024

The thesis of Samuel Brandt was reviewed and approved by the following:

John M. Peters
Assistant Professor of Meteorology and Atmospheric Science
Thesis Advisor

Matthew R. Kumjian
Professor of Meteorology and Atmospheric Science

Jerry Y. Harrington
Professor of Meteorology
Head of Graduate Program in Meteorology

ABSTRACT

Supercells are perhaps the most organized form of thunderstorm, with structure that persists over relatively long periods of time. Part of this persistent structure is a feature referred to as the “rear flank downdraft” (RFD). There is a bevy of prior research on short duration downdraft surges in this region, but ample room for a dynamic understanding of the persistence of RFDs exists. Bulk analysis of numerous trajectories within simulations of supercells across environments with varied shear and lifted condensation level (LCL) shows that reductions in the vertical perturbation pressure gradient acceleration (VPPGA) are primarily responsible for the downward acceleration of near-surface downdrafts in the RFD region. Time averaged and updraft centered composites suggest that linear dynamic VPPGA resulting from interactions between environmental vertical wind shear and the low-level supercell updraft explain the persistence of the RFD region. A technique is presented to compare the potential for linearly forced supercell RFD between environments using a vertical wind profile.

TABLE OF CONTENTS

LIST OF FIGURES

LIST OF TABLES

ACKNOWLEDGEMENTS

I would like to thank my advisor, Dr. John Peters, for not just guiding me through my master's degree but also teaching me how to be an effective scientist. I am also greatly appreciative of the rest of my committee for steering this thesis in the right direction, and the other graduate students in my research group for always being willing to help along the way. Lastly, I want to thank my family for being so supportive of my aspirations in meteorology for such a long time; it's hard for me to imagine getting to this point without them.

This thesis was supported by NSF and DOE grants AGS-2149353, DE-SC0022942, and DE-89243020SSC000051. The findings and conclusions of this thesis do not necessarily reflect the views of these agencies.

Chapter 1

Introduction

I. Background

Downdrafts are downward moving air currents. When downdrafts produced by thunderstorms reach the surface, they are forced via mass continuity to spread out horizontally producing gusty winds, sometimes fast enough to endanger life and property. The most intense variety of thunderstorm is the supercell, consisting "primarily of a single, quasi-steady rotating updraft" (American Meteorological Society 2024) and they can produce a wide variety of severe weather hazards including tornadoes, large hail, and damaging wind gusts (Markowski 2007, Blair et al. 2017). "Quasi-steady" refers to storm structures that are persistent over long periods of time. Near-surface downdrafts are routinely observed in a quasi-steady region of supercells referred to as the "rear-flank downdraft", or RFD (Markowski 2002). RFDs have long been hypothesized to play a substantial role in the formation of supercell tornadoes (Markowski 2002), with a radar feature known as a "descending reflectivity core" garnering outsized interest in this area (Rasmussen et al. 2006, Kennedy et al. 2007, Byko et al. 2009). Localized downdraft surges often occur within the RFD region over short time scales (Wurman et al. 2007b, Marquis et al. 2008, Skinner et al. 2014) and can contribute to locally intense wind damage.

II. Downdraft Acceleration

Whereas nonsupercell downdrafts are primarily accelerated downward by condensate drag (Torri and Kuang 2016) and negative thermal buoyancy (Heus and Jonker 2008, Glenn and Krueger 2013), scattered evidence across past literature suggests that supercell downdrafts –

particularly in the RFD region – are primarily driven by dynamic pressure accelerations. Kumjian (2011) hypothesized that dynamically driven RFDs could explain why rain drop size distributions in that region of supercells can contain abnormally large concentrations of small drops relative to other convective regimes; these downdrafts could transport small rain drops to the ground faster than their terminal fall speed giving them less time than otherwise to evaporate. Marion and Trapp (2019) showed that the horizontal area of supercell updrafts was strongly correlated with downdraft area. Various acceleration terms of the vertical velocity equation were correlated to updraft area, however vertical velocity budgets for the downdrafts were not explicitly analyzed. In addition, Marion and Trapp (2019) focused on downdrafts at a height of 3.25 km, which may have been too high to capture downdrafts with direct impacts at the surface. Klemp and Rotunno (1983) did investigate the vertical velocity budgets for near-surface downdrafts in a simulated supercell and found that specifically during the occlusion phase, downdrafts locally accelerated downwards towards low pressure resulting from the intensification of near-surface vertical vorticity. However, this mechanism cannot be extended to explain near-surface supercell downdrafts that occur outside of an occlusion. An observational study of a tornadic supercell by Johnson et al. (1987) utilized a multi-Doppler radar retrieval to conclude that downdraft trajectories began between 0-2 km above the ground to the east of the storm, ascended to 1-4.5 km, then descended to the west of the rotating updraft into the RFD. Like Klemp and Rotunno (1983), they found evidence of a downward directed vertical perturbation pressure gradient acceleration (VPPGA) in the lowest few hundred meters above the ground coincident with the downdrafts, however no physical mechanism was proposed to explain its existence. The consensus among many studies reviewed by Markowski (2002) was that negative buoyancy (from gas-phase density perturbations due to evaporation and/or melting of precipitation; condensate drag) was the likely source of downward acceleration for supercell downdrafts, though Nelson (1977) suggested that dynamic perturbation pressure may play at least a partial role. Markowski

(2002) cited the limits of radar observations as a tool for understanding supercell downdrafts in the RFD region: “A lack of data due to the pristine air common in RFD regions probably still is one of the biggest obstacles in understanding the formation mechanisms and the role of the RFD today.” This limitation naturally leads to numerical simulation as a particularly effective avenue for exploring RFD dynamics, and that is precisely what Schenkman et al. (2016) did. They performed a simulation of a supercell based on a tornado case from 8 May 2003 in Oklahoma City and investigated the vertical velocity budget of a few RFD trajectories. Outflow surges in the RFD region were found to be forced by the dynamic part of the VPPGA, and examinations of vertical cross sections revealed that high perturbation pressure coincident with “stagnating flow” located on the WNW flanks of the lower-level (below 3 km) mesocyclone was the culprit. They noted that this high perturbation pressure region was quite unsteady and determined that later, colder RFD outflow surges were buoyantly forced. While these insights explain the dynamics of RFD surges, they do not explain the general persistence of the RFD over time scales much longer than individual surges, nor do they elucidate the impacts that varying environmental conditions may have on RFD dynamics.

III. Research Motivation

There are four primary aspects of Schenkman et al. (2016) that will be expanded upon by this study:

1) The vertical velocity budgets of individual trajectories were analyzed with the aim of explaining downdraft surges; this study will investigate large sample sizes of near-surface supercell downdraft trajectories with the aim of investigating quasi-steady downdraft structure.

2) The perturbation pressure field was decomposed into dynamic and buoyant contributions; I will be further decomposing dynamic perturbation pressure into two sub-categories.
3) There was a focus on outflow surges i.e., downdrafts occurring on short time scales; This study will shift its focus to the more persistent downdraft structure present in the RFD region of supercells.
4) One supercell environment was considered; I will simulate multiple supercells in systematically varied environments to investigate how certain environmental parameters may or may not affect RFD behavior.

The goal of this thesis is to create a more complete dynamical understanding of why persistent near-surface downdraft structure exists in the RFD region of supercells over a range of environments. To do this, I will leverage the advantages of numerical simulation over radar observations to analyze large sample sizes of Lagrangian downdraft parcel trajectories for supercells over a range of environments. In addition, storm-centered time composites will be used to determine a physical mechanism for quasi-steady downdraft structure. My hypothesis is that the linear component of dynamic perturbation pressure is primarily responsible for persistent downdraft structure in the rear-flank region of supercells, with buoyancy playing a minimal role. I expect linear dynamic VPPGAs to dominate quasi-steady downdraft structure because of the term's dependence on the base state vertical wind profile interacting with perturbation vertical velocity. Since supercells are comprised of a persistent updraft, the linear VPPGAs resulting from the base state vertical wind profile interacting with the updraft should also be quasi-steady; this motivates varying the base state vertical wind profile across the simulations. I will also be varying the lifted condensation level (LCL) of the environment. Markowski et al. (2002) concluded that environments with larger LCLs (and correspondingly lower boundary layer relative humidity) were associated with larger near-surface negative buoyancy in the RFD regions of observed

supercells than in environments with smaller LCLs. If buoyancy is indeed not a significant contributor to near-surface quasi-steady supercell downdrafts, then varying the environmental LCL should not change their dynamics.

Chapter 2

Methodology

I. General Simulation Information

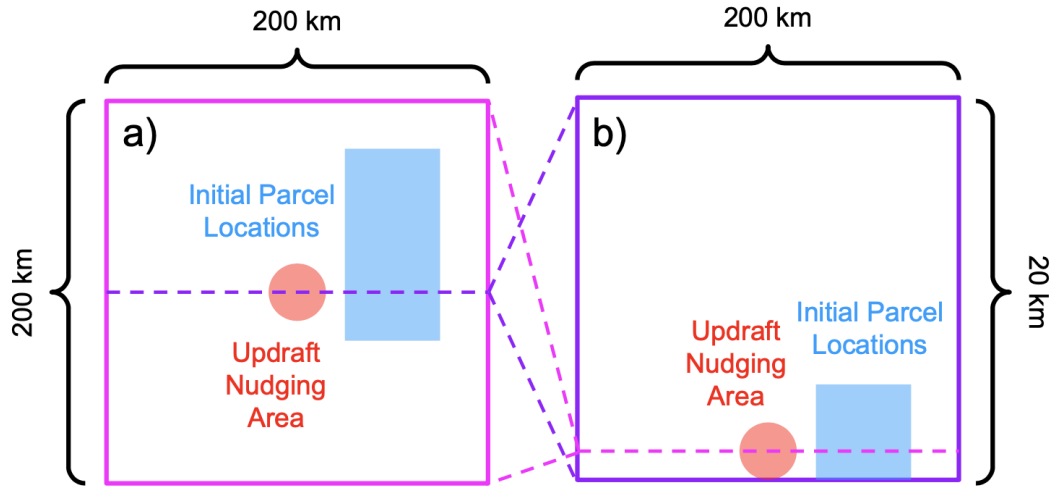

Figure **1**: Visual summary in the x-y plane (panel a) and x-z plane (panel b) of the simulation domain and the initial locations of updraft nudging (red) and Lagrangian parcel trajectories (blue) to scale. The dotted line in panel a corresponds to panel b's cross section and vice versa.

Cloud Model version 1, release 21.0 (CM1; Bryan and Fritsch 2002) was used to perform six simulations of supercell thunderstorms. Each simulation was performed within a 200x200x20 km domain partitioned into a Cartesian grid with 250-m horizontal grid spacing and 100-m vertical grid spacing. The lateral boundary conditions were chosen to be open radiative, and the top and bottom boundaries were free slip. Discrete supercells were initiated using an area of updraft nudging following Naylor and Gilmore (2012) at the bottom-center of the domain (Figure 1) using code built into CM1; values used for the various parameters of the updraft nudging implementation are listed in Table 1. A constant horizontal grid translation corresponding to the

estimated supercell motion from the Bunkers hodograph technique (Bunkers et al. 2000) was applied to keep simulated right-moving supercells closer to the center of the model domain. In addition to solving on the grid, over a quarter-million Lagrangian parcel trajectories were initialized upstream of eventual near-surface downdrafts in the RFD region, arranged in regular intervals of 1 km in the horizontal and 50 m in the vertical according to the blue shaded areas of Figure 1. These trajectories were run in-line with the rest of the simulation, again using code built into CM1. Air parcel properties following these trajectories were output every 15 s. The Morrison and Gettleman double-moment microphysics scheme (Morrison and Gettleman 2008) was employed for these simulations. It is acknowledged that as shown by Murzdek et al. (2022), choice of microphysical parameterization can incur large variability in the cold pool characteristics of convective storm simulations, especially in environments with large lifted condensation levels (LCLs). This sensitivity is most relevant to buoyant contributions to downdraft accelerations. The details of the CM1 configuration are summarized by Table 1.

Table 1: CM1 Configuration

Parameter	**Value**
Domain Size	200x200x20 km
Horizontal Grid Spacing	250 m
Vertical Grid Spacing	100 m
Initial Large Time Step	0.7 s
Lateral Boundary Conditions	Open Radiative
Top and Bottom Boundary Conditions	Free Slip
Initiation Method	Updraft Nudging
Horizontal Radius of Nudging	15 km
Vertical Radius of Nudging	1.5 km
Inverse e-Folding Time for Nudging (alpha)	0.5 1/s
Max w to Nudge Towards	10 m/s
Times to Ramp Down and Turn Off Nudging	900 and 1200 s
Microphysics	Morrison Two Moment
Radiation	None
Surface Fluxes	None
Coriolis Accelerations	None
Grid Output Frequency	300 s
Trajectory Output Frequency	15 s

Table 1: Summary of the CM1 configuration parameters used.

II. Systematic Varying of Base State

To test the influence of a supercell's environment on downdraft characteristics, two properties of the base state vertical profile were systematically varied: LCL and the "deep layer shear" magnitude (to be defined later). Thermodynamic vertical profiles were constructed for three LCLs: 500 m, 1000 m, and 2000 m. These were designed in such a way as to keep undiluted convective available potential energy (CAPE; calculated using the adiabatic method described in Peters et al. 2022), surface moist static energy (MSE), and free tropospheric relative humidity (TRH) approximately constant at values of 2500 J kg^{-1}, 325000 J kg^{-1}, and 33%, respectively. Holding CAPE and TRH constant was done to ensure that simulated updrafts achieved similar magnitudes, and holding MSE constant was done to ensure that updraft parcels existed over equivalent temperature ranges (since MSE is theoretically conserved for lifted parcels), mitigating any updraft differences due to microphysical processes with strong temperature dependencies. MSE is defined by Eq. 1 (Neelin and Held 1987),

(1) $$MSE = DSE + L_v q_v$$

where L_v is the enthalpy of vaporization, q_v is the water vapor mass fraction, and DSE is the dry static energy, defined by Eq. 2 (Neelin and Held 1987):

(2) $$DSE = c_p T + gz$$

where c_p is the specific heat capacity of air, T is the temperature, g is acceleration due to gravity, and z is height. At the LCL, MSE takes the form of Eq. 3:

(3) $$MSE = DSE + L_v q_v{}^*(T_{LCL})$$

where $q_v{}^*(T_{LCL})$ is the equilibrium ("saturated") water vapor mass fraction at T_{LCL}, the temperature at the height of the LCL. From the surface to the LCL, the DSE of a lifted parcel is conserved, leading to Eq. 4:

(4) $$c_p T_{sfc} = c_p T_{LCL} + g \cdot LCL$$

where the LHS of Eq. 4 is the DSE at the surface (with T_{sfc} being the surface temperature) and the RHS of Eq. 4 is the DSE at the LCL. Eq. 4 can be rearranged to solve for T_{LCL} and plugged into Eq. 3, and the LHS of Eq. 4 can be substituted for DSE in Eq. 3 yielding Eq. 5:

(5) $$MSE = c_p T_{sfc} + L_v q_v{}^* \left(T_{sfc} - \frac{g}{c_p} LCL \right)$$

For a given LCL and MSE, Eq. 5 can be solved for T_{sfc}. The corresponding surface water vapor mass fraction $q_{v,sfc}$ can then be determined via Eq. 6:

(6) $$MSE = c_p T_{sfc} + L_v q_{v,sfc}$$

After determining the surface temperature and water vapor mass fraction, the rest of the thermodynamic vertical profile was constructed using the methods of Peters et al. (2024) with a constant CAPE of 2500 J kg^{-1}, which generates a buoyancy profile inputs of surface temperature, surface RH, CAPE, and TRH using composite buoyancy profiles from the severe thunderstorm proximity sounding dataset of Thompson et al. (2003).

Kinematic vertical profiles were constructed according to piecewise functions with respect to height z (in m) for east/west u wind (Eq. 7; in m s^{-1}) and north/south v wind (Eq. 8; in m s^{-1}). These functions take inspiration from the "quarter circle" wind profiles of Rotunno and Klemp (1982) but have been modified to be expressed in terms of LCL and have a quarter ellipse shape beneath the LCL rather than a quarter circle.

(7) $$u(z) = \begin{cases} -\frac{c_1}{4} \cos\left(\frac{\pi z}{2LCL}\right) & z \leq LCL \\ c_2(z - LCL) & LCL < z \leq LCL + 5000 \\ 5000 c_2 & z > LCL + 5000 \end{cases}$$

(8) $$v(z) = \begin{cases} c_1 \sin\left(\frac{\pi z}{2LCL}\right) & z \leq LCL \\ c_1 & z > LCL \end{cases}$$

The c_1 parameter in Eqs. 7 and 8 was held constant at a value of 10 m s^{-1}. A consequence of this choice is that the shear below the LCL will be strongest/weakest for the lowest/highest LCLs. This choice is justified by considering that higher LCL environments have deeper turbulently

mixed boundary layers that act to suppress vertical wind shear and vice versa. The c_2 parameter in Eq. 7, which will be referred to as "deep layer shear", was given two possible values: 0.005 1/s and 0.008 1/s. The three thermodynamic profiles with varied LCLs and two kinematic profiles with varied deep layer shear were combined into a 3x2 matrix of six base state vertical profiles within which supercells were simulated (Figure 2). Individual simulations will be referenced throughout the results by the following naming convention: XLCL_Yshear, where X is the LCL in m, and Y is the deep layer shear magnitude in 1/s with the leading zero and decimal point omitted. Each panel of Figure 2 is titled with its name following this convention.

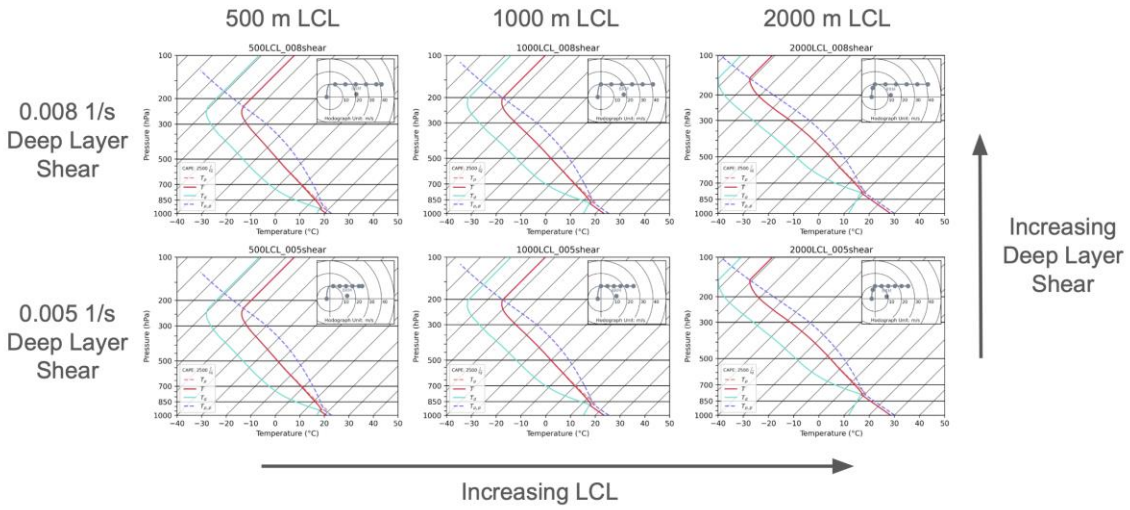

Figure 2: 3x2 matrix of skew-T and hodograph diagrams depicting base state vertical profiles for the supercell simulations. LCL height is varied by column and deep-layer shear (the c_2 parameter in Eq. 1) is varied by row. The red, dotted red, cyan, and dotted purple lines in the skew-T plots correspond to base state temperature, base state density temperature, base state dewpoint temperature, and lifted parcel density temperature respectively. Circular markers on the hodographs delineate each km of height. CAPE, surface moist static energy, free tropospheric relative humidity, and the c_1 parameter as defined in Eqs. 7 and 8 are held constant.

III. Downdraft Identification

Trajectories containing strong downdrafts near the ground needed to be algorithmically identified. To this end, a trajectory needed to meet four thresholds to be counted:

1) A height (z) below 500 m; this ensures that the identified downdrafts are those that most directly impact the surface. The precise value of 500 m is somewhat arbitrary, but results did not change for height thresholds between 250 and 1000 m.
2) A vertical velocity (w) less than -5 m s^{-1}; this was done to prevent weak downdrafts due to turbulent eddies from contaminating samples.
3) Occurring at least 40 minutes into the simulation; this ensures that simulated supercells have had plenty of time to achieve a quasi-steady state after the updraft nudging process. A special truncated time range was applied to one of the simulations that only managed transient supercell structure, illustrated by the darkest gray shading in Figure 3.
4) Occurring south of y = +30000 m (30 km north of the model domain's center); this filters out downdrafts associated with any left-moving storms that developed and was determined via trial-and-error.

Minor changes to these four thresholds yielded similar qualitative results, so values were settled on with the aim of maximizing sample sizes.

IV. Vertical Velocity Budget

Vertical velocity budgets along downdraft trajectories were analyzed according to Eq. 9 (Cotton and Anthes 1989),

$$\frac{Dw}{Dt} = g\frac{\theta-\theta_0}{\theta_0} + g\left(\frac{R_v}{R_d} - 1\right)(r_v - r_{v0}) - g(r_t - r_v) - c_p\theta_\rho\frac{\partial \Pi'}{\partial z} + residuals. \quad (9)$$

Eq. 9 is the exact equation used by CM1 to compute vertical accelerations. From left to right, the terms are

1) trajectory vertical acceleration ($\frac{Dw}{Dt}$)
2) buoyancy due to dry air effects on density (where θ and θ_0 are trajectory and base state potential temperature, respectively, and g is acceleration due to gravity)
3) buoyancy due to water vapor effects on density (i.e., the "virtual temperature effect" described in Doswell and Rasmussen 1994, where R_v and R_d are the water vapor and dry air gas constants, respectively, and r_v and r_{v0} are the trajectory and base state water vapor mixing ratios, respectively)
4) buoyancy due to condensate drag (where r_t is the total mixing ratio of water vapor and condensate)
5) VPPGA expressed in terms of the Exner function (Π) to fully remove perturbation pressure from the buoyancy term (Cotton and Anthes 1989, where c_p is the specific heat capacity of the air and θ_ρ is the density potential temperature)
6) Residuals from parameterized turbulence and numerical dampening. In practice, the residuals were vanishingly small compared to the buoyancy and VPPGA terms and were thus ignored.

Condensing the three buoyancy terms into one yields the buoyancy portion of the vertical velocity budget that is outputted by CM1 along trajectories, and together with the VPPGA will constitute the two terms of the vertical velocity budget that will be considered for analysis. While individual trajectories depict instantaneous accelerations, averaging a large sample of downdraft trajectories together over long periods of time reveals the quasi-steady nature of the vertical velocity budgets.

V. Time Composites

A method was needed for approximating the quasi-steady structure around a supercell. This was accomplished by finding the location of the maximum 5 km updraft and centering a 50x50 km grid on that location for each output time. The 5 km updraft location was found by taking the average location of any grid cells with vertical velocity exceeding the 99^{th} percentile of the 2-D slice in the x-y plane at 5 km for the given output time. Updraft-centered velocity fields were then averaged over many output times and the result was interpreted as quasi-steady state structure. Any additional calculations requiring the velocity fields, like dynamic VPPGA forcing terms, were done on the time-averaged fields.

Chapter 3

Results

I. Updraft Characteristics

Every simulation produced a quasi-steady, intense updraft apart from 500LCL_005shear which yielded transient supercell structure that decayed over time (Figure 3, dark red line). The remaining five quasi-steady storms sustained maximum vertical velocities near or just below the theoretical maximum predicted by CAPE (Figure 3). Maximum updraft magnitudes for those 5 simulations became indistinguishable from each other after about an hour of simulated time, a sign that environmental variables outside of LCL and deep layer shear were well controlled for.

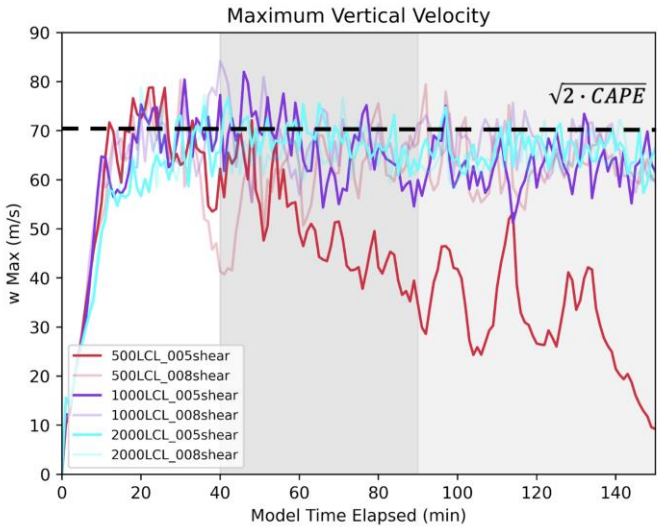

Figure 3: Time series of maximum vertical velocity (y-axis, m s^{-1}) for each simulation, with elapsed model time in minutes shown on the x-axis. The period enclosed by gray shading is the range of times over which downdraft trajectories were identified according to the third threshold explained in Section 2. Likewise, the darker gray shading indicates the special truncated time range for the transient supercell produced by the 500LCL_005shear simulation. The black dotted line corresponds to the theoretical maximum vertical velocity achievable by a parcel with 2500 J kg^{-1} of CAPE beginning at rest, equal to the square root of twice the CAPE.

II. Downdraft Characteristics

The downdraft identification methodology described in Section 2 was successful in collecting large sample sizes (Figure 4). Distributions of downdraft intensity were qualitatively similar across all six simulations, though some quantitative differences in percentile thresholds were present (Figure 4). Despite this, no consistent trends were evident across the rows or columns of the simulation matrix (Figure 4), suggesting that varying the LCL and deep layer shear did not meaningfully contribute to downdraft intensity.

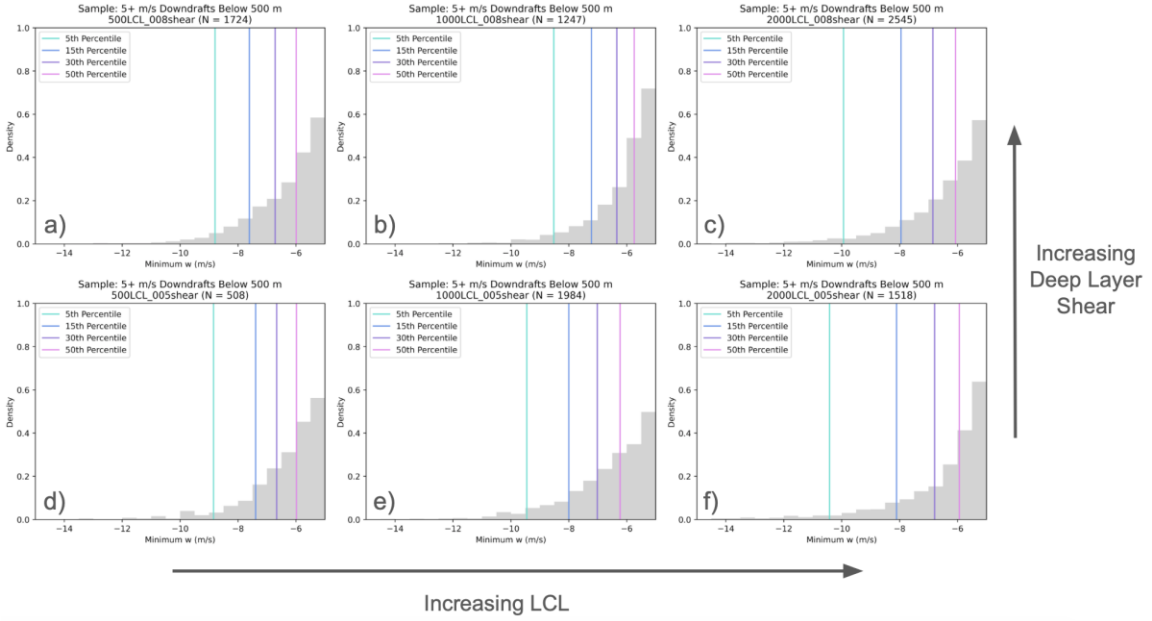

Figure 4: Normalized histograms of the minimum vertical velocity (x-axes, m s^{-1}) achieved below 500 m for each simulation. The size of the downdraft sample for each simulation, collected according to the thresholds outlined in Section 2, is denoted by "N =" in each panel title. 5^{th}, 15^{th}, 30^{th}, and 50^{th} percentile minimum vertical velocities are drawn as colored vertical lines and labeled in the legend of each panel.

Most trajectories began below the LCL, slowly rose to 50%-130% of the LCL in the minutes leading up to the downdraft, then rapidly descended to near the ground (Figure 5). Just

25% of downdraft trajectories originated above the LCL (Figure 5). Maximum downward accelerations generally occurred a minute or two prior to the downdraft thresholds being reached and around the height of the LCL (Figure 5). Accelerations occurring at those heights, therefore, must have been especially important for near-surface downdraft development.

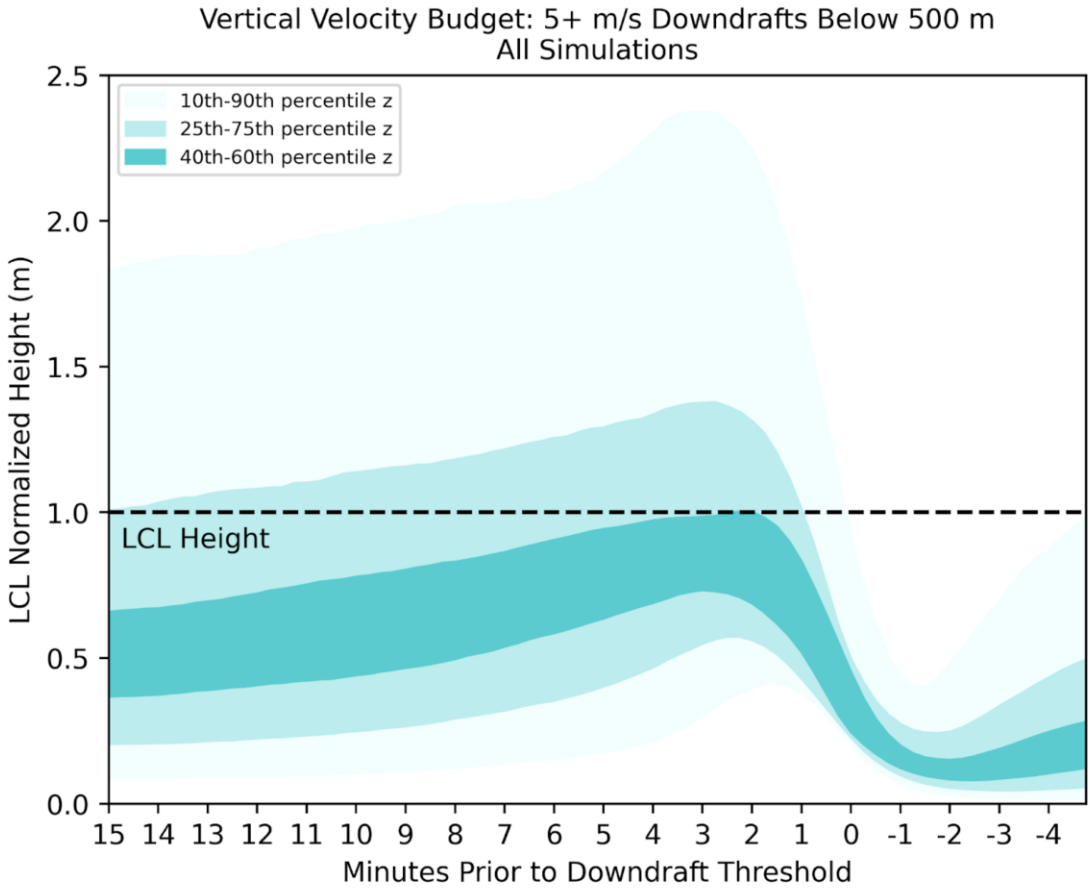

Figure 5: Time series of downdraft trajectory heights across all simulations. The x-axis corresponds to number of minutes prior to the downdraft thresholds outlined in Section 2 being met, and the y-axis corresponds to the height of the trajectory, normalized by the LCL of each simulation (and therefore dimensionless). The dotted black line corresponds to the height of the LCL. Shaded regions corresponding to the middle 80%, 50%, and 20% of trajectories are denoted by progressively darker shades of blue.

All six simulations featured a cluster of downdrafts to the west of their supercell's updraft in the RFD region (Figure 6). In most of the simulations, these RFD clusters constituted a majority of the downdrafts in the sample, save for the 1000LCL_008shear simulation (Figure 6b). The combined results of Figures 5 and 6 imply that downdrafts meeting Section 2's thresholds accelerated primarily to the west of parent updrafts at or just below the height of the LCL. Therefore, any physical explanation of these downdraft trajectory patterns needs to be consistent with those locations.

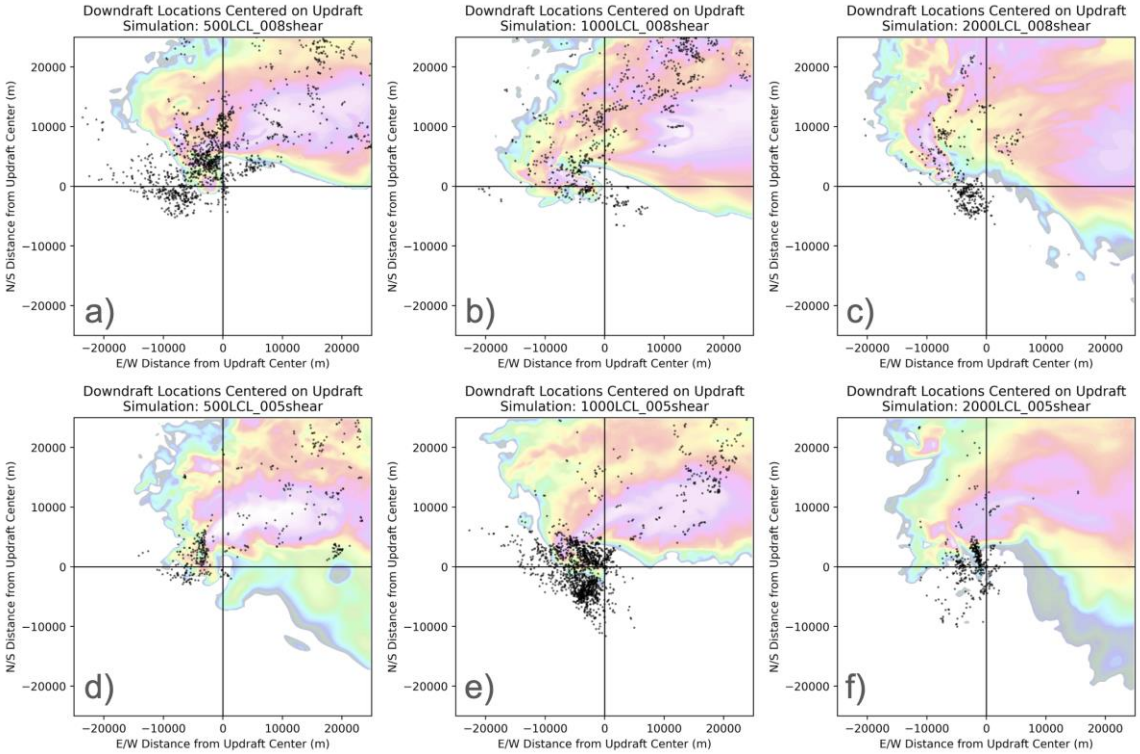

Figure 6: Scatterplots of downdraft locations meeting the thresholds from Section 2 in the horizontal plane (x and y-axes both in m) for each simulation, with the origin of each panel representing the location of the maximum 4-6 km updraft at the time of each downdraft. Instantaneous simulated radar reflectivity at 1 km from an arbitrary output time is plotted for context with a consistent color scale for each panel.

III. Vertical Velocity Budgets

The processes driving downward acceleration were qualitatively similar across all six simulations. 10+ minutes prior to reaching the thresholds, downdraft trajectories were in hydrostatic balance (note from Figure 7 that the total vertical acceleration was essentially zero at those times). Three minutes prior to the downdraft threshold being reached, the VPPGA drastically decreased (with the exception of Figure 7c), throwing the trajectories out of hydrostatic balance with a downward net acceleration (Figure 7). In the minutes immediately following the downdrafts, the VPPGA spiked back up (Figure 7) to accelerate the vertical velocity to zero as the downdrafts hit the ground, upholding mass continuity. During the downdrafts, small increases in buoyancy were noted in the 500 m and 1000 m LCL simulations (Figure 7, columns a-d and b-e) possibly due to adiabatic compressional warming of trajectories as they descended. This feature was not noted in the 2000 m LCL simulations (Figure 7, column c-f). Despite similar net accelerations across the six simulations there were some minor quantitative differences, particularly with the 1000 m and 2000 m cases (Figure 7, columns b-e and c-f) which featured larger negative buoyancy post-downdraft. The sample mean VPPGA in the 2000LCL_008shear simulation (Figure 7c) did not bottom out below zero like in the other five; a relative decrease in the VPPGA's magnitude along with steadily decreasing buoyancy was the catalyst for downward accelerations.

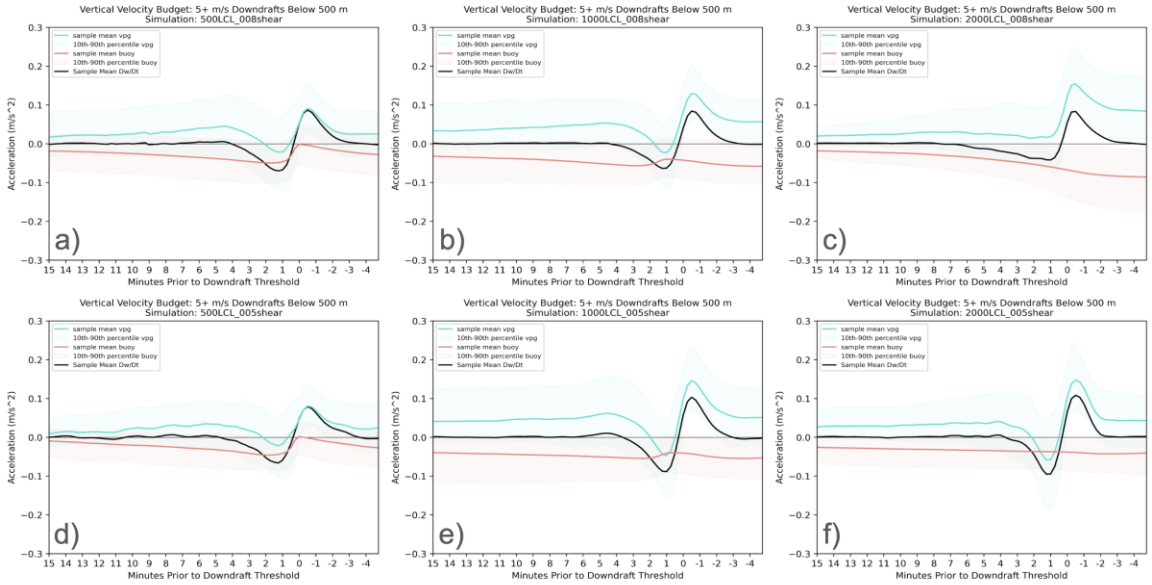

Figure 7: Mean vertical velocity budgets (y-axis, m s^{-2}) for the downdraft samples meeting the thresholds stated in Section 2, using the same downdraft-relative x-axes as in Figure 5. Sample mean buoyancy/VPPGA are plotted as solid red/cyan lines respectively, with colored shading representing the corresponding 10^{th}-90^{th} percentile ranges. Sample mean net vertical accelerations approximated as the sum of buoyancy and VPPGA are plotted as black lines.

Across all six simulations, supercell downdraft intensity exhibited a correlation to the minimum VPPGA (Figure 8, blue histograms) that was much larger than the corresponding minimum buoyancy (Figure 8, red histograms). In every simulation expect for 1000LCL_008shear (Figure 8b), the minimum buoyancy exhibited a small negative correlation to downdraft intensity. Adding the minimum buoyancy accelerations to the minimum VPPGAs only marginally improved the correlations to downdraft intensity (Figure 8, purple histograms). Clearly, VPPGAs played an outsized role in the acceleration of strong near-surface downdrafts across the six supercell simulations.

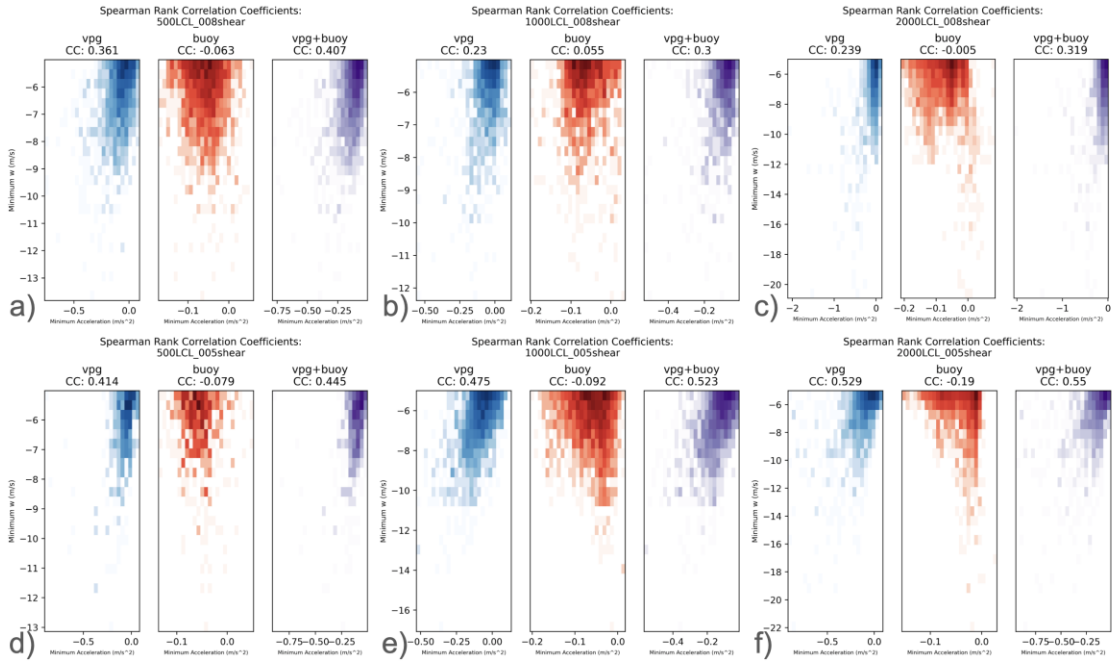

Figure 8: 2-D histogram plots of minimum VPPGA (blue), buoyant acceleration (red), and total acceleration (purple) prior to a downdraft on the x-axes (all in m s^{-2}) and the minimum vertical velocity of the eventual downdraft on the y-axes (in m s^{-1}). Logarithmic color scales were used to better highlight the shape of the distributions at higher downdraft intensities. Spearman rank correlation coefficients were used to quantify the correlations between minimums in the acceleration terms and eventual minimum vertical velocity and labeled as "CC:" in the title of each subplot.

IV. Physical Mechanisms

Reductions in the VPPGA 1) to the west of supercell updrafts and 2) at or just below the height of the LCL were overwhelmingly responsible for bulk downdraft behavior, but that raises the question "What caused the reduced VPPGA"? The answer begins with Eq. 10 describing the perturbation pressure field, derived by Rotunno and Klemp (1982) and written in the format found in Gray and Frame (2019):

$$\frac{1}{\rho_0}\nabla^2 p' = -\left(e'_{ij}\right)^2 + \frac{1}{2}\left|\overrightarrow{\omega'}\right|^2 - 2\vec{S}\cdot\nabla_h w + \frac{\partial b}{\partial z} \quad (10)$$

The symbols and physical meanings of terms in Eq. 10 are defined by Tables 2 and 3 respectively:

Table 2: Pressure Equation Symbols

Symbol	Meaning	Units
ρ_0	Hydrostatically balanced base state density	$kg \cdot m^{-3}$
∇^2	3-D Laplacian operator	m^{-2}
p'	Perturbation pressure from hydrostatic base state	$kg \cdot m^{-1} \cdot s^{-2}$
e'_{ij}	Deformation tensor of perturbation velocity field	s^{-1}
$\left\|\overrightarrow{\omega'}\right\|$	Magnitude of 3-D vorticity of perturbation velocity field	s^{-1}
$\vec{S}$	Vertical gradient of the base state horizontal wind	s^{-1}
∇_h	Horizontal gradient operator	m^{-1}
w	Vertical velocity	$m \cdot s^{-1}$
$\frac{\partial}{\partial z}$	Vertical gradient	m^{-1}
b	Buoyancy	$m \cdot s^{-2}$

Table 2: Definitions of symbols in Eq. 10.

Table 3: Pressure Equation Terms

Term	Meaning
$\frac{1}{\rho_0}\nabla^2 p'$	**3-D Laplacian of perturbation pressure**; describes how the perturbation pressure field "responds" to forcing terms on the other side of the equation.
$-\left(e'_{ij}\right)^2$	**Deformation Term**: Square of the deformation tensor of the perturbation velocity field; describes how the velocity field is "stretching" and "warping" fluid elements. This term always contributes to positive perturbation pressure.
$\frac{1}{2}\left\|\overrightarrow{\omega'}\right\|^2$	**Vorticity Term**: Square of the magnitude of the 3-D vorticity vector; describes how fluid elements are spinning. This term always contributes to a negative perturbation pressure.
$-2\vec{S}\cdot\nabla_h w$	**Linear Term**: The dot product of shear of the base state horizontal wind with the horizontal gradient of vertical velocity; describes how wind shear interacts with updrafts and downdrafts. This term contributes to positive perturbation pressure on the upshear flank of an updraft, and negative perturbation pressure on the downshear flank of an updraft.
$\frac{\partial b}{\partial z}$	**Buoyancy Term**: The vertical gradient of buoyancy; describes how buoyancy changes with height. This term contributes to positive perturbation pressure where buoyancy is decreasing with height and contributes to negative perturbation pressure where buoyancy is increasing with height.

Table 3: Physical meanings of the various terms of Eq. 10.

Next, a modification to Eq. 10 will be made to convert it from an equation for perturbation pressure into an equation describing VPPGA. To do this, Eq. 10 is multiplied by negative one, the reference density is moved inside the 3-D Laplacian operator (essentially making a Boussinesq approximation), and the vertical gradient of the entire equation is taken. Performing these operations results in Eq. 11.

$$\nabla^2\left(-\frac{1}{\rho_0}\frac{\partial p\prime}{\partial z}\right) = \nabla^2(VPPGA) = \frac{\partial\left({e\prime_{ij}}^2\right)}{\partial z} - \frac{1}{2}\frac{\partial\left(\left|\overrightarrow{\omega\prime}\right|^2\right)}{\partial z} + 2\frac{\partial(\vec{S}\cdot\nabla_h w)}{\partial z} - \frac{\partial^2 b}{\partial z^2} \quad (11)$$

For conceptual purposes, the Laplacian operator can be treated as proportional to a negative sign, leading to Eq. 12.

$$VPPGA \propto -\frac{\partial\left({e\prime_{ij}}^2\right)}{\partial z} + \frac{1}{2}\frac{\partial\left(\left|\overrightarrow{\omega\prime}\right|^2\right)}{\partial z} - 2\frac{\partial(\vec{S}\cdot\nabla_h w)}{\partial z} + \frac{\partial^2 b}{\partial z^2} \quad (12)$$

Eq. 12 describes the possible mechanisms for a negative VPPGA. The first term and second terms on the RHS of Eq. 12 constitute the non-linear dynamic part of VPPGA forcing; either deformation of the perturbation velocity field increasing with height or vorticity of the perturbation velocity field decreasing with height (like in the occlusion downdrafts described by Klemp and Rotunno 1983) will contribute to a downward non-linear dynamic VPGGA. The third term on the RHS of Eq. 12 represents the linear dynamic part of VPPGA forcing. Finally, a negative second derivative of buoyancy with respect to height will contribute to a downward VPPGA.

Quasi-steady state composites of LCL vertical velocity (Figure 9) are consistent with the trajectory location results in Figure 6, exhibiting a persistent downdraft to the west of updrafts. Supercell updrafts became progressively wider with both increasing deep layer shear inducing stronger storm-relative inflow (Warren et al. 2017, Peters et al. 2019b, Marion and Trapp 2019) and increasing LCL height (McCaul and Cohen 2002, Mulholland et al. 2021) (Figure 9). Linear forcing for VPPGAs was consistent with the requirements for a quasi-steady state supercell RFD

mechanism; forcing for downward accelerations consistently occurred to the west of low-level updrafts at the height of the LCL (Figure 10). The magnitude of the downward linear VPPGA forcing appeared to be strongest in the simulations that produced the widest updrafts (Figures 10b, 10c, 10f). Non-linear forcing for downward VPPGAs was much less consistent among the simulations in quasi-steady state composites (Figure 11). A few simulations hint at quasi-steady structure relevant to RFD production (blue horseshoe patterns in Figures 11b, 11c, and blue strip to the south of the updraft in Figure 11e); I speculate that this is due to horizontal vorticity baroclinically produced along the rear flank gust front decreasing with increasing height.

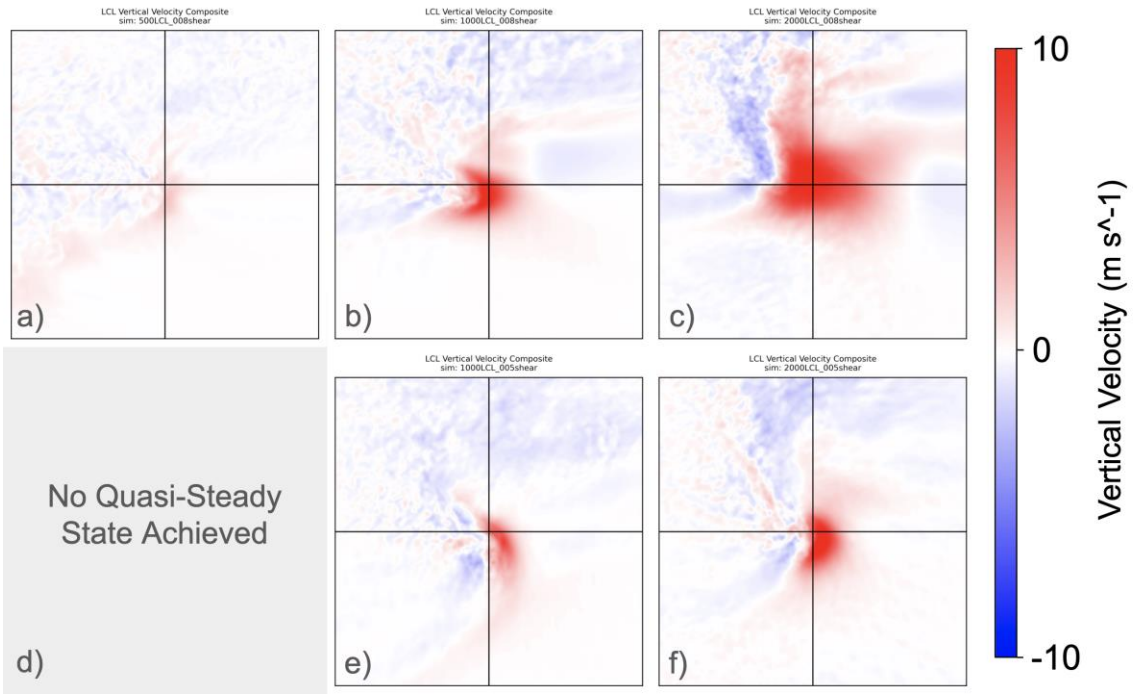

Figure 9: Time-averaged composites in the x-y plane over a period of 90 minutes of vertical velocity at the height of each simulation's LCL, centered on the 5 km maximum updraft and extending 25 km in each cardinal direction. Red areas signify positive vertical velocities and blue areas signify negative vertical velocities over a range of -10 m s^{-1} to +10 m s^{-1}. Because no quasi-steady state was achieved by the 500LCL_005shear simulation (panel d), its composite was not considered.

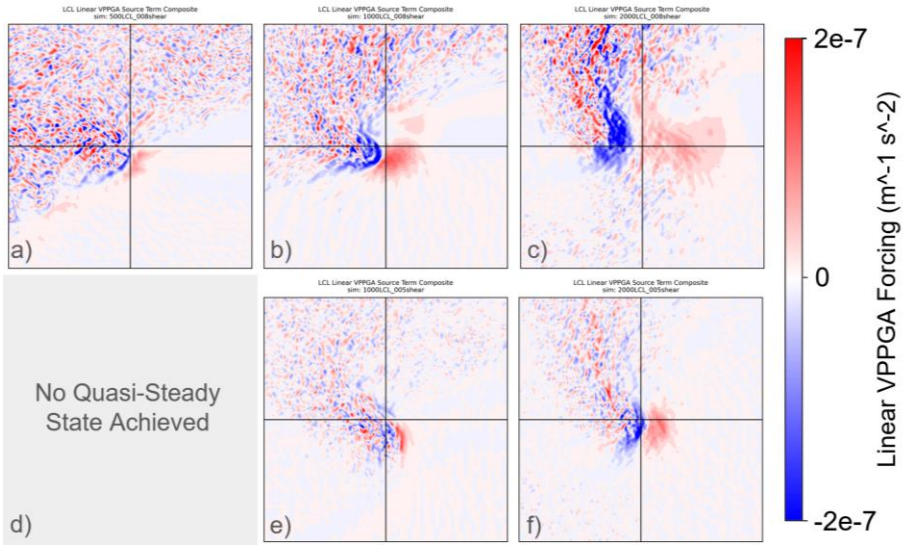

Figure 10: The linear dynamic forcing term for VPPGA at the height of the LCL in the x-y plane calculated on quasi-steady state composites of the vertical velocity field, centered on the 5 km maximum updraft and extending 25 km in cardinal each direction. Red areas signify forcing for upward VPPGAs and blue areas signify forcing for downward VPPGAs.

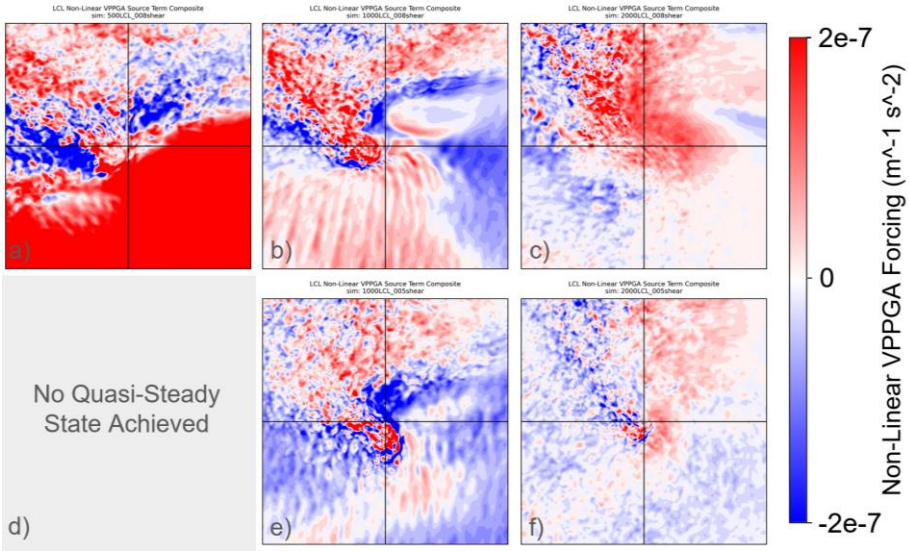

Figure 11: The non-linear dynamic forcing term for VPPGA at the height of the LCL in the x-y plane calculated on quasi-steady state composites of the 3-D velocity field, centered on the 5 km maximum updraft and extending 25 km in each cardinal direction. Red areas signify forcing for upward VPPGAs and blue areas signify forcing for downward VPPGAs.

V. Discussion and Application

Taken together, Figures 10 and 11 imply that while non-linear dynamic VPPGA forcing may sometimes be important on short time scales (for example the occlusion downdrafts described by Klemp and Rotunno 1983), when focusing on quasi-steady state downdraft structure the linear dynamic VPPGA forcing term becomes ubiquitous and explains why supercells tend to have persistent downdrafts in their rear flank region. Schenkman et al. (2016) did not decompose dynamic VPPGAs into linear and non-linear components, but it is plausible that the "stagnation high pressure" they found at 1.5 km above the ground in a vertical cross section (their Figure 13) was induced by linear dynamic forcing based on its position relative to the supercell's updraft. The fact that linear forcing plays such an important role in supercell downdraft structure is great news for operational meteorology, as linear forcing can be compared between environments using just a vertical wind profile. Take the linear term of Eq. (12):

$$VPPGA \propto -2\frac{\partial(\vec{S}\cdot\nabla_h w)}{\partial z}, \tag{13}$$

where

$$\vec{S} = \frac{\partial u_0}{\partial z}\hat{\imath} + \frac{\partial v_0}{\partial z}\hat{\jmath} \tag{14}$$

is the vertical shear of the base state horizontal wind $u_0(z)\hat{\imath} + v_0(z)\hat{\jmath}$. Using the product rule of calculus, the RHS of Eq. (13) can be expanded into

$$VPPGA \propto -2\left(\frac{\partial\vec{S}}{\partial z}\cdot\nabla_h w + \vec{S}\cdot\nabla_h\frac{\partial w}{\partial z}\right). \tag{15}$$

Next, it will be assumed that the vertical velocity field can be approximated as

$$w(x,y,z) = z\frac{\partial w}{\partial z}(x,y), \tag{16}$$

where $\frac{\partial w}{\partial z}(x,y)$ is an arbitrary function of x and y alone (i.e., $\frac{\partial w}{\partial z}$ can vary in the horizontal but is constant with respect to height z) describing the vertical divergence. The assumption that vertical velocity increases approximately linearly with height beneath deep convective updrafts of all

kinds is supported by Figure 1b of Schiro et al. 2018 (tropical convection in weak shear) and Figure 12 (supercells in strong shear):

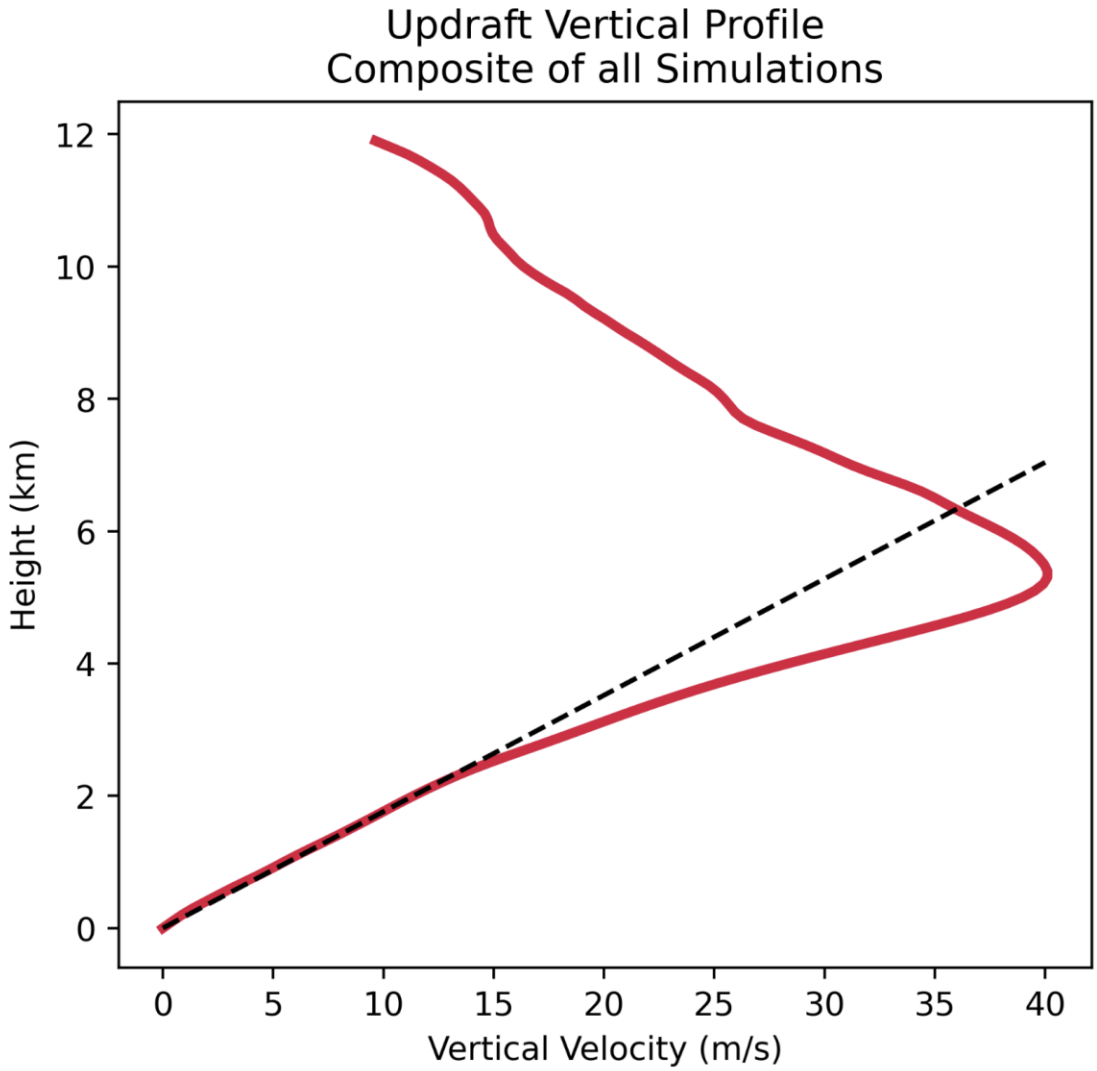

Figure 12: Profile of vertical velocity (x-axis, m s^{-1}) with respect to height (y-axis, km) within vertical slices corresponding to maximum 5 km updrafts averaged over all simulations plotted in red. The black dotted line corresponds the linear increase in vertical velocity with height that best matches the profile in the lowest 2 km.

Especially in the lower part of the updraft where linear forcing is most important for near-surface supercell RFDs, vertical velocity increases linearly to good approximation (Figure 12, Schiro et al. 2018 Figure 1b). Substituting Eq. 16 into the first term on the RHS of Eq. 15 yields Eq. 17:

(17) $$VPPGA \propto -2\left(\frac{\partial \vec{S}}{\partial z} \cdot z\nabla_h \frac{\partial w}{\partial z} + \vec{S} \cdot \nabla_h \frac{\partial w}{\partial z}\right).$$

Eq. 17 can be rearranged into

(18) $$VPPGA \propto -2\left(\frac{\partial \vec{S}}{\partial z} z + \vec{S}\right) \cdot \nabla_h \frac{\partial w}{\partial z}.$$

The term inside the parenthesis on the right-hand side of Eq. 18 is proportional to the linear forcing for VPPGA (all else related to the $\nabla_h \frac{\partial w}{\partial z}$ term being equal) and its magnitude is straightforward to compute from an environmental vertical wind profile. This can be done using Eq. 19:

(19) $$|VPPGA(z)| \propto \sqrt{\left[\frac{\partial^2(u_0(z))}{\partial z^2} z + \frac{\partial(u_0(z))}{\partial z}\right]^2 + \left[\frac{\partial^2(v_0(z))}{\partial z^2} z + \frac{\partial(v_0(z))}{\partial z}\right]^2}$$

Where $u_0(z)$ and $v_0(z)$ are the east/west and north/south components of the base state wind profile, and z is the height above the ground. The first and second derivatives with respect to height can be calculated using finite difference approximations. For Figure 13, second-order (also known as "centered") finite difference approximations were used to evaluate Eq. 19.

Figure 13 applies Eq. 19 to two observed vertical wind profiles associated with tornadic supercells. Large hodograph curvature in the OAX sounding around 1 km above the ground (Figure 13d) contributes to a large linear VPPGA forcing (Figure 13c). Conversely, modest hodograph curvature below 2 km in the FFC sounding (Figure 13b) contributes to smaller linear VPPGA forcing. When evaluated around the height of the LCL, this technique may provide forecasters useful information on which environments are more or less supportive of strong downdrafts in supercells, with the important caveat that the $\nabla_h \frac{\partial w}{\partial z}$ term is assumed to be constant.

So, Eq. 19 really answers the question “Given a particular quasi-steady supercell updraft, which vertical wind profile will interact with it to produce larger linear forcing for downdrafts”?

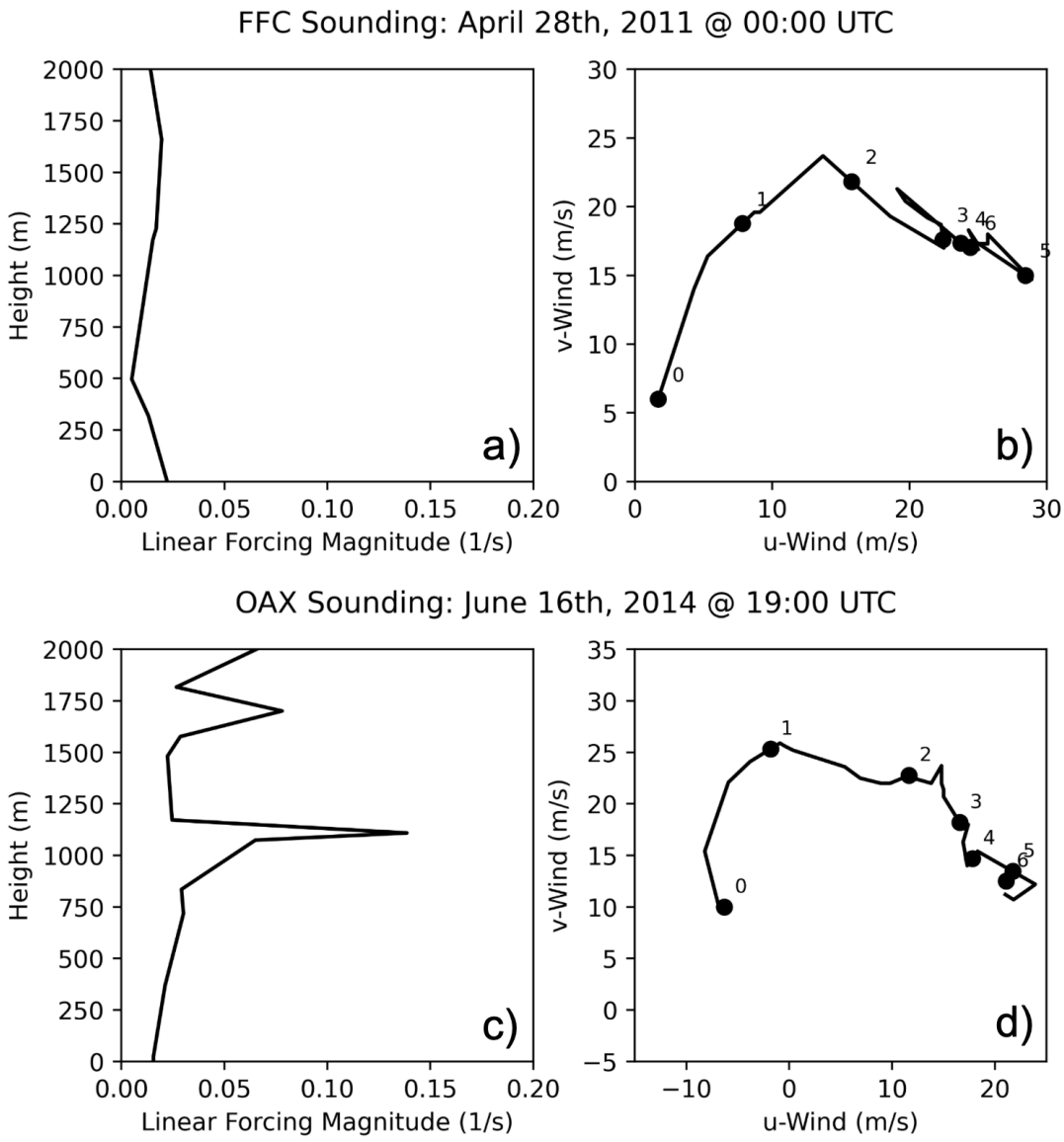

Figure 13: Two observed vertical wind profiles associated with significant (EF-2+) tornadoes. Each row corresponds to a specific vertical wind profile; hodographs are plotted in the right column (E-W wind component in m s^{-1} on the x-axis, N-S wind component in m s^{-1} on the y-axis, height markers every km), and the calculation of Eq. 19 is plotted in the left column (forcing magnitude in 1/s on the x-axis, height in m on the y-axis).

Chapter 4

Summary and Conclusion

Across six simulations of supercell thunderstorms in environments with varied LCLs and deep-layer shear, vertical perturbation pressure gradient accelerations were found to be the primary driver of near-surface downdrafts. The strongest downdrafts tended to occur to the west of supercell updrafts in the rear flank region, and for the most part those trajectories started below the storm's environmental LCL. Linear forcing due to environmental vertical wind shear interacting with horizontal gradients in vertical velocity was determined to be the primary physical mechanism responsible for persistent downdraft structure in the rear flank region, though across shorter time scales non-linear forcing may contribute. Relative magnitudes of linear forcing can be estimated from environmental vertical wind profiles, providing forecasters a method to ascertain a supercell environment's propensity for strong RFDs.

References

American Meteorological Society, 2024: Supercell, Glossary of Meteorology, http://glossary.ametsoc.org/wiki/Supercell.

Blair, S. F., and Coauthors, 2017: High-Resolution Hail Observations: Implications for NWS Warning Operations. *Wea. Forecasting*, **32**, 1101–1119, https://doi.org/10.1175/WAF-D-16-0203.1.

Bryan, G. H., and J. M. Fritsch, 2002: A Benchmark Simulation for Moist Nonhydrostatic Numerical Models. *Mon. Wea. Rev.*, **130**, 2917–2928, https://doi.org/10.1175/1520-0493(2002)130<2917:ABSFMN>2.0.CO;2.

Bunkers, M. J., B. A. Klimowski, J. W. Zeitler, R. L. Thompson, and M. L. Weisman, 2000: Predicting Supercell Motion Using a New Hodograph Technique. *Wea. Forecasting*, **15**, 61–79, https://doi.org/10.1175/1520-0434(2000)015<0061:PSMUAN>2.0.CO;2.

Byko, Z., P. Markowski, Y. Richardson, J. Wurman, and E. Adlerman, 2009: Descending Reflectivity Cores in Supercell Thunderstorms Observed by Mobile Radars and in a High-Resolution Numerical Simulation. *Wea. Forecasting*, **24**, 155–186, https://doi.org/10.1175/2008WAF2222116.1.

Cotton, W. R., & Anthes, R. A. (1989). Fundamental Equations Governing Cloud Processes. In *Storm and Cloud Dynamics* (pp. 30-32). Academic press.

Doswell , C. A., and E. N. Rasmussen, 1994: The Effect of Neglecting the Virtual Temperature Correction on CAPE Calculations. *Wea. Forecasting*, **9**, 625–629, https://doi.org/10.1175/1520-0434(1994)009<0625:TEONTV>2.0.CO;2.

Gray, K., and J. Frame, 2019: Investigating the Transition from Elevated Multicellular Convection to Surface-Based Supercells during the Tornado Outbreak of 24 August 2016 Using a WRF Model Simulation. *Wea. Forecasting*, **34**, 1051–1079, https://doi.org/10.1175/WAF-D-18-0209.1.

Johnson, K. W., P. S. Ray, B. C. Johnson, and R. P. Davies-Jones, 1987: Observations Related to the Rotational Dynamics of the 20 May 1977 Tornadic Storms. *Mon. Wea. Rev.*, **115**, 2463–2478, https://doi.org/10.1175/1520-0493(1987)115<2463:ORTTRD>2.0.CO;2.

Kennedy, Aaron D., Erik N. Rasmussen, and Jerry M. Straka. "A visual observation of the 6 June 2005 descending reflectivity core." *E-Journal of Severe Storms Meteorology* 2.6 (2007): 1-12. https://doi.org/10.55599/ejssm.v2i6.11

Klemp, J. B., and R. Rotunno, 1983: A Study of the Tornadic Region within a Supercell Thunderstorm. *J. Atmos. Sci.*, **40**, 359–377, https://doi.org/10.1175/1520-0469(1983)040<0359:ASOTTR>2.0.CO;2.

Kumjian, M. R., 2011: Precipitation properties of supercell hook echoes. *Electron. J. Severe Storms Meteor.*, **6** (5).

Marion, G. R., & Trapp, R. J. (2019). The dynamical coupling of convective updrafts, downdrafts, and cold pools in simulated supercell thunderstorms. *Journal of Geophysical Research: Atmosphere*, **124**(2), 664–683. https://doi.org/10.1029/2018JD029055

Markowski, P. M., 2002: Hook Echoes and Rear-Flank Downdrafts: A Review. *Mon. Wea. Rev.*, **130**, 852–876, https://doi.org/10.1175/1520-0493(2002)130<0852:HEARFD>2.0.CO;2.

Markowski, P. M., J. M. Straka, and E. N. Rasmussen, 2002: Direct Surface Thermodynamic Observations within the Rear-Flank Downdrafts of Nontornadic and Tornadic Supercells. *Mon. Wea. Rev.*, **130**, 1692–1721, https://doi.org/10.1175/1520-0493(2002)130<1692:DSTOWT>2.0.CO;2.

Markowski, P. (2007). Supercell Thunderstorms. In: Giaiotti, D.B., Steinacker, R., Stel, F. (eds) Atmospheric Convection: Research and Operational Forecasting Aspects. CISM International Centre for Mechanical Sciences, vol 475. Springer, Vienna. https://doi.org/10.1007/978-3-211-69291-2_5

Marquis, J., Y. Richardson, J. Wurman, and P. Markowski, 2008: Single- and Dual-Doppler Analysis of a Tornadic Vortex and Surrounding Storm-Scale Flow in the Crowell, Texas, Supercell of 30 April 2000. *Mon. Wea. Rev.*, **136**, 5017–5043, https://doi.org/10.1175/2008MWR2442.1.

McCaul, E. W., and C. Cohen, 2002: The Impact on Simulated Storm Structure and Intensity of Variations in the Mixed Layer and Moist Layer Depths. *Mon. Wea. Rev.*, **130**, 1722–1748, https://doi.org/10.1175/1520-0493(2002)130<1722:TIOSSS>2.0.CO;2.

Morrison, H., and A. Gettelman, 2008: A New Two-Moment Bulk Stratiform Cloud Microphysics Scheme in the Community Atmosphere Model, Version 3 (CAM3). Part I: Description and Numerical Tests. *J. Climate*, **21**, 3642–3659, https://doi.org/10.1175/2008JCLI2105.1.

Mulholland, J. P., J. M. Peters, and H. Morrison. "How does LCL height influence deep convective updraft width?." *Geophysical Research Letters* 48.13 (2021): e2021GL093316. **https://doi.org/10.1029/2021GL093316**

Murdzek, S. S., Y. P. Richardson, P. M. Markowski, and M. R. Kumjian, 2022: How the Environmental Lifting Condensation Level Affects the Sensitivity of Simulated Convective Storm Cold Pools to the Microphysics Parameterization. *Mon. Wea. Rev.*, **150**, 2527–2552, https://doi.org/10.1175/MWR-D-21-0258.1.

Naylor, J., and M. S. Gilmore, 2012: Convective Initiation in an Idealized Cloud Model Using an Updraft Nudging Technique. *Mon. Wea. Rev.*, **140**, 3699–3705, https://doi.org/10.1175/MWR-D-12-00163.1.

Neelin, J. D., and I. M. Held, 1987: Modeling Tropical Convergence Based on the Moist Static Energy Budget. *Mon. Wea. Rev.*, **115**, 3–12, https://doi.org/10.1175/1520-0493(1987)115<0003:MTCBOT>2.0.CO;2.

Nelson, S. P., 1977: Rear flank downdraft: A hailstorm intensification mechanism. Preprints, *10th Conf. on Severe Local Storms*, Omaha, NE, Amer. Meteor. Soc., 521–525.

Peters, J. M., C. J. Nowotarski, and H. Morrison, 2019: The Role of Vertical Wind Shear in Modulating Maximum Supercell Updraft Velocities. *J. Atmos. Sci.*, **76**, 3169–3189, https://doi.org/10.1175/JAS-D-19-0096.1.

Peters, J. M., J. P. Mulholland, and D. R. Chavas, 2022: Generalized Lapse Rate Formulas for Use in Entraining CAPE Calculations. *J. Atmos. Sci.*, **79**, 815–836, https://doi.org/10.1175/JAS-D-21-0118.1.

Rasmussen, E. N., J. M. Straka, M. S. Gilmore, and R. Davies-Jones, 2006: A Preliminary Survey of Rear-Flank Descending Reflectivity Cores in Supercell Storms. *Wea. Forecasting*, **21**, 923–938, https://doi.org/10.1175/WAF962.1.

Rotunno, R., and J. B. Klemp, 1982: The Influence of the Shear-Induced Pressure Gradient on Thunderstorm Motion. *Mon. Wea. Rev.*, **110**, 136–151, https://doi.org/10.1175/1520-0493(1982)110<0136:TIOTSI>2.0.CO;2.

Schenkman, A. D., M. Xue, and D. T. Dawson II, 2016: The Cause of Internal Outflow Surges in a High-Resolution Simulation of the 8 May 2003 Oklahoma City Tornadic Supercell. *J. Atmos. Sci.*, **73**, 353–370, https://doi.org/10.1175/JAS-D-15-0112.1.

Schiro, K. A., F. Ahmed, and D. J. Neelin, 2018: GoAmazon2014/5 campaign points to deep-inflow approach to mesoscale-organized and unorganized deep convection. *Proc. Natl. Acad. Sci. USA*, **115**, 4577–4582, https://doi.org/10.1073/pnas.1719842115.

Skinner, P. S., C. C. Weiss, M. M. French, H. B. Bluestein, P. M. Markowski, and Y. P. Richardson, 2014: VORTEX2 Observations of a Low-Level Mesocyclone with Multiple Internal Rear-Flank Downdraft Momentum Surges in the 18 May 2010 Dumas, Texas, Supercell. *Mon. Wea. Rev.*, **142**, 2935–2960, https://doi.org/10.1175/MWR-D-13-00240.1.

Thompson, R. L., R. Edwards, J. A. Hart, K. L. Elmore, and P. Markowski, 2003: Close Proximity Soundings within Supercell Environments Obtained from the Rapid Update Cycle. *Wea. Forecasting*, **18**, 1243–1261, https://doi.org/10.1175/1520-0434(2003)018<1243:CPSWSE>2.0.CO;2.

Warren, R. A., Richter, H., Ramsay, H. A., Siems, S. T., & Manton, M. J. (2017). Impact of variations in upper-level shear on simulated supercells. *Monthly Weather Review*, **145**(7), 2659–2681. https://doi.org/10.1175/MWR-D-16-0412.1

Wurman, J., Y. Richardson, C. Alexander, S. Weygandt, and P. F. Zhang, 2007: Dual-Doppler Analysis of Winds and Vorticity Budget Terms near a Tornado. *Mon. Wea. Rev.*, **135**, 2392–2405, https://doi.org/10.1175/MWR3404.1.